coatings

MDPI

Article

Improving Optical and Electrical Characteristics of GaN Films via 3D Island to 2D Growth Mode Transition Using Molecular Beam Epitaxy

Thi Thu Mai [1], Jin-Ji Dai [1], Wu-Ching Chou [1,*], Hua-Chiang Wen [1], Le Trung Hieu [2] and Huy Hoang Luc [3,*]

[1] Department of Electrophysics, National Yang Ming Chiao Tung University, Hsinchu 30010, Taiwan; maithucs@gmail.com (T.T.M.); jinjidai@gmail.com (J.-J.D.); a091316104@gmail.com (H.-C.W.)
[2] Wide Bandgap Compound Semiconductor Research Center, Industry Academia Innovation School, National Yang Ming Chiao Tung University, Hsinchu 30010, Taiwan; hieult@nycu.edu.tw
[3] Faculty of Physics, Hanoi National University of Education, 136 Xuan Thuy, Cau Giay, Hanoi 123105, Vietnam
* Correspondence: wcchou957@nycu.edu.tw (W.-C.C.); hoanglhsp@hnue.edu.vn (H.H.L.); Tel.: +886-3-5712121-56129 (W.-C.C.); +84-903200023 (H.H.L.)

Abstract: Molecular beam epitaxy (MBE) is demonstrated as an excellent growth technique for growing a low-defect GaN channel layer, which is crucial for controlling vertical leakage current and improving breakdown voltage (BV) in GaN-based high-electron mobility transistors (HEMTs). The 3D islands to 2D growth mode transition approach was induced by modulating substrate growth temperature (Tsub), displaying an overall improvement in film quality. A comprehensive investigation was conducted into the effects of Tsub on surface morphologies, crystal quality, and the optical and electrical properties of GaN films. Optimal results were achieved with a strain-relaxed GaN film grown at 690 °C, exhibiting significantly improved surface characteristics (root-mean-square roughness, Rq = 0.3 nm) and impressively reduced edge dislocations. However, the film with the smoothest surface roughness, attributed to the effect of the Ga-rich condition, possessed a high surface pit density, negatively affecting optical and electrical properties. A reduction in defect-related yellow emission further confirmed the enhanced crystalline quality of MBE GaN films. The optimized GaN film demonstrated outstanding electrical properties with a BV of ~1450 V, surpassing that of MOCVD GaN (~1180 V). This research significantly contributes to the advancement of MBE GaN-based high electron mobility transistor (HEMT) applications by ensuring outstanding reliability.

Keywords: 3D-to-2D growth; MBE; GaN HEMT; vertical leakage; breakdown voltage; dislocations

check for updates

Citation: Mai, T.T.; Dai, J.-J.; Chou, W.-C.; Wen, H.-C.; Hieu, L.T.; Luc, H.H. Improving Optical and Electrical Characteristics of GaN Films via 3D Island to 2D Growth Mode Transition Using Molecular Beam Epitaxy. *Coatings* **2024**, *14*, 191. https://doi.org/10.3390/coatings14020191

Academic Editor: Andrey V. Osipov

Received: 13 January 2024
Revised: 27 January 2024
Accepted: 31 January 2024
Published: 1 February 2024

Copyright: © 2024 by the authors. Licensee MDPI, Basel, Switzerland. This article is an open access article distributed under the terms and conditions of the Creative Commons Attribution (CC BY) license (https://creativecommons.org/licenses/by/4.0/).

1. Introduction

GaN-on-Si-based high-electron mobility transistors (HEMTs) possess unique advantages for applications demanding high power and frequency due to their outstanding characteristics, such as high breakdown voltage (BV), excellent thermal stability, lower on-state resistance, high electron saturation velocity, and low cost [1,2]. However, crucial technological challenges remain due to the mismatches in lattice parameters and the coefficient of thermal expansion (CTE) between GaN and Si [3]. These issues limit the device's ultimate performance, resulting from the involvement of current collapse phenomena, high density of threading dislocations (TDD) (10^9–10^{10} cm^{-2}), and excessive residual strains [4,5]. The current collapse phenomenon arises from charge traps in the undoped (UID) GaN layer, which subsequently accumulated near the interface of two-dimensional electron gas (2DEG) at the AlGaN/GaN heterostructure, and from the GaN buffer layer, which deleteriously causes power losses [6]. These traps are frequently identified in MOCVD-grown GaN films due to the incorporation of undesirable impurity-related defects (such as carbon, oxygen, or silicon) during growth [7]. Moreover, dislocations pose a substantial risk, contributing to an increase in leakage current and sheet resistance of 2DEG and also reducing BV and

free carrier mobility [8,9]. Hence, contemporary efforts to enhance HEMT devices focus on minimizing interfacial impurity accumulation and reducing dislocations to minimize power losses. Additionally, carefully managing the GaN structure thickness also requires particular attention for mitigating micro-cracks and wafer curvature while improving the breakdown field. Several approaches have been proposed to address these issues, including implementing thick strain-relief stacks (SRSs) and interlayers. These approaches encompass the mitigating stress buffer layers [10], super-lattice buffer layers [11], step-graded AlN/AlGaN [12], low-temperature LT-AlN and SiNx interlayers [13,14], 3D-to-2D growth mode transition [14,15], and epitaxial lateral overgrowth (ELOG) [16,17]. However, while addressing certain issues, the thick SRS can introduce a notable drawback of severe cracking and wafer bowing arising from the over-thickening effects of highly strained epitaxial films [18]. The minimum thickness for high-quality GaN HEMT structures with a TDD of ~10^9 cm^{-2} is typically around 6 μm [12]. Techniques involving interlayers, or ELOG, can generate nanomasks to facilitate the transition from 3D to 2D growth mode but may negatively affect device performance, including increasing vertical leakage current [19], cracking issues, and interrupted dislocation propagation in regions lacking mask contribution [17]. In contrast, the molecular beam epitaxy (PA-MBE) technique has shown remarkable breakthroughs in improving device performance. This technique produces high-pure epitaxial films at ultra-high vacuum, low growth temperatures, and optimal stoichiometric growth conditions [20–23]. Specifically, MBE-grown GaN homoepitaxial films in Ga-rich conditions have resulted in excellent film quality [20,21]. Zhang et al. [20] found that higher nitrogen flows led to a better crystal quality of homoepitaxial GaN films but also resulted in an undesirable rough surface. Surface roughness critically impacts carrier mobility, parasitic resistance, and the presence of negative deep traps [24,25]. Smooth surface morphologies are attainable when films are grown in the Ga droplet and intermediate regimes. However, the devices still exhibited inferior electron transport density and luminescence properties owing to the Ga droplet effect [26,27]. Controlling substrate growth temperature (Tsub) allows for the efficient desorption of excessive Ga atoms on the surface while effectively incorporating them into GaN films, which is facilitated by supplying adequate thermal energy for surface activation during coalescence [21,28]. However, excessive substrate thermal energy can lead to surface over-desorption, resulting in rough surface morphology and deteriorating the film quality. Conversely, insufficient desorption temperature may cause Ga droplet issues [27]. Thus far, there has been limited study of employing MBE for promoting 3D-to-2D growth mode transitions. Furthermore, a comprehensive study of the electrical characteristics of MBE-grown GaN films under growth mode transition is essential.

In this study, high-quality UID GaN layers on MOCVD GaN/Si (111) templates were obtained using MBE growth. This accomplishment involved implementing a 3D to 2D growth mode transition by adjusting Tsub under Ga-rich conditions. The effects of the growth mode transition on the surface morphologies, defect reduction, crystal quality, and optical and electrical characteristics of the MBE-grown GaN films compared with MOCVD GaN templates have been investigated. The findings of this work provide valuable insights for future research on the manufacturing of highly reliable GaN-based devices.

2. Materials and Methods

Figure 1a illustrates the schematic structure of MBE GaN film on MOCVD GaN/Si (111) templates. The templates were deposited by MOCVD on 6-inch Si (111) wafers, consisting of a 200 nm AlN nucleation layer followed by a 280 nm $Al_{0.25}Ga_{0.75}N$ layer. The 800 nm C-doped GaN insulating buffer layer was then grown to reduce defect-induced residual electrons. The final deposited layer was a 300 nm UID GaN layer. The 2×2 cm^2 GaN/Si templates were cut and cleaned with acetone, isopropyl alcohol, and deionized water (DI). The cleaned templates were then transferred into the growing chamber, which was followed by an in situ thermal cleaning process under an ultra-high vacuum (4.0×10^{-11} Torr) at 150 °C for 30 min in order to eliminate surface organic contaminants

and native oxides. Subsequently, the MBE UID GaN films were processed at various Tsub of 670 °C (Sample A), 680 °C (Sample B), 690 °C (Sample C), and 700 °C (Sample D). Sample X refers to the MOCVD GaN/Si template. During the growth process, active nitrogen species were maintained at a flow rate of 0.6 sccm using an SVT radio-frequency plasma source operating at a constant RF-plasma power of 300 W. A standard gallium (Ga) dual-filament effusion cell was utilized to deliver thermal evaporation of the Ga precursor with an imposing flux of 6.70×10^{-7} Torr. Real-time monitoring of epitaxial film quality along the $(11\bar{2}0)$ azimuth was conducted via reflection high-energy electron diffraction (RHEED) powered by a 12 keV electron gun with a set filament current of 1.5 µA. The thickness of the MBE GaN films was approximately 300 nm ± 10 nm, which was measured using a JSM7001F scanning electron microscope (SEM), as shown in Figure 1b. The sample surface morphologies were studied using atomic force microscopy (AFM) and SEM measurements. X-ray diffraction (XRD) examination was carried out employing a Bruker D2 PHASER using CuKα X-ray source radiation (λ = 0.15406 nm). The scanning range of 2 theta (2θ) spanned from 10 to 80° with a scan rate of 0.03° s^{-1}, a slit width of 0.1 mm, and an exposure period of 0.2 s. High-resolution XRD of Bede D1 using CuKα radiation provided information on dislocation densities in GaN that were evaluated from the full width at half maximum (FWHM) of the ω-rocking curves of the (002) and (102) reflections. Optical characteristics were obtained utilizing Raman and photoluminescence (PL) examinations. The PL measurement was carried out using a 325 nm He-Cd laser excitation source. The room-temperature Raman measurement was performed using an Argon ion laser with a wavelength of 514 nm and a power of 50 mW. Room-temperature vertical leakage–voltage (I-V) characterization was conducted through the floating substrate with a top metal of 74×74 µm^2 Ti/Al/Ni/Au stack, which was followed by the formation of ohmic contact using rapid thermal annealing at 800 °C for 60 s in a nitrogen atmosphere.

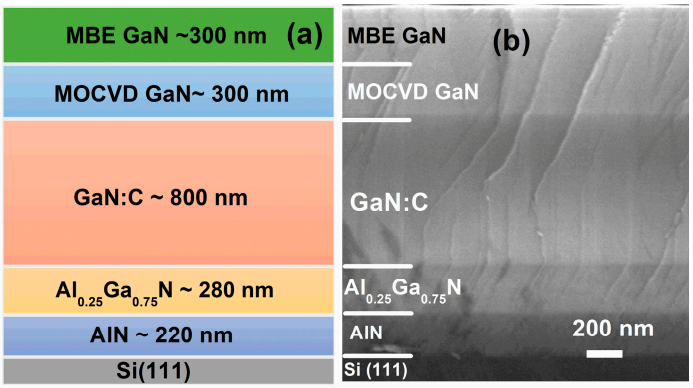

Figure 1. (**a**) Schematic diagram of MBE GaN film grown on MOCVD GaN/Si templates. (**b**) Cross-sectional SEM image of the GaN film.

3. Results and Discussion

3.1. Surface Reconstruction and Morphology Analysis

Figure 2 displays the captured RHEED patterns illustrating surface reconstruction of the GaN film at varying Tsub. Throughout the Tsub range up to 660 °C, the 2×2 streaky RHEED patterns of GaN templates were observed [Figure 2a inset]. Subsequently, as Tsub increased from 670 to 700 °C, the RHEED patterns evolved into spotty features with slight increases in size and intensities (Figure 2a–d). This transformation indicates the formation of the predominant three-dimensional (3D) islands on the surface of the GaN templates [29]. The initially spotty RHEED patterns then underwent an immediate transition into 1×1 streaky RHEED reconstruction shortly after the initiation of homoepitaxial growth. The rapid recovery of RHEED patterns indicates a transition from 3D islands to 2D growth modes, suggesting the achievement of smooth surface morphologies in MBE GaN [30]. These consistent streaky RHEED patterns persisted during the growth of samples A, B, and C (Figure 2e–g). Typically, the 1×1 streaky RHEED features are associated with

GaN films grown under the Ga-stable condition, which are characterized by Ga-rich and intermediate regimes where excessive Ga atoms on the surface manifest as Ga metallic droplet regions or wet regions [22,31]. It is evident that the RHEED characteristics are significantly affected by modulating Tsub. Notably, Sample A (Tsub = 670 °C) exhibited dimmed RHEED patterns, indicating the GaN film went through the Ga droplet regime. With the increasing Tsub, the streaky RHEED patterns of samples B and C became brighter, signifying well-desorbed excessive Ga atoms on the film surface. Conversely, persistence in spotted RHEED patterns with heightened intensities was observed during the growth of sample D (Tsub = 700 °C), indicating the adherence of the grown film to a 3D growth mode. The spotty RHEED features are acknowledged for creating a high surface roughness. This observation highlights the crucial role of modulating Tsub in facilitating the transition from 3D islands to 2D growth mode, thereby contributing to the preservation of smooth surface morphologies. The transition from streaky to spotty RHEED patterns has been reported as a function of substrate temperatures and the Ga/N ratio [31]. Hence, we infer that maintaining a growth temperature below 700 °C is essential to prevent over-desorption and provide a smooth film surface. For simplicity of the analysis and to emphasize the improved properties of GaN films, we primarily studied samples A, B, and C and compared them with sample X.

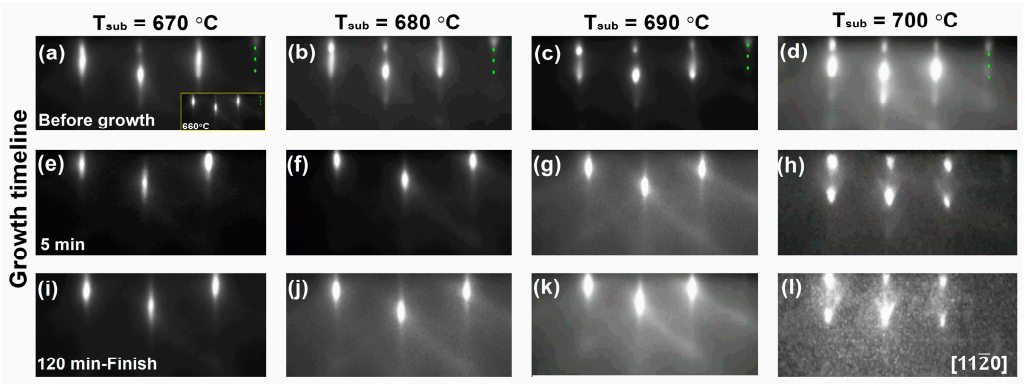

Figure 2. In situ RHEED patterns evolution of GaN films recorded at (**a**–**d**) different substrate temperatures of 670 °C, 680 °C, 690 °C, and 700 °C respectively; (**e**–**h**) after 5 minutes of deposition; and (**i**–**l**) immediately after growth completions. Insets in Figure 2a show RHEED patterns of GaN at a substrate temperature of 660°C.

The variation of surface roughness and pit densities (PD) of MBE GaN films with Tsub was explored using SEM and AFM examinations, as displayed in Figure 3. For reference, the AFM image of the template is also provided in Figure 3d. The relation between root mean square (Rq) and average PDs estimated relatively from SEM images is given in Figure 3h. The results revealed that the 3D-to-2D growth mode transition greatly improved the surface morphologies of MBE films, resulting in a decreased Rq relative to sample X (Rq = 0.50 nm). Sample A (Tsub = 670 °C) displayed an Rq of 0.18 nm, which was attributed to the lower surface desorption energy of Ga atoms during coalescence, enabling comparatively smooth surface morphology due to Ga droplets. However, the existence of excessive Ga atoms can be accompanied by the formation of nitrogen vacancies, thereby inducing a high surface pit density of ~2.12×10^9 cm^{-2}. As Tsub is raised to 680 °C and 690 °C, enhanced substrate thermal energy facilitates a more effective surface desorption of Ga atoms. This phenomenon resulted in a substantial decrease in surface pit densities. For sample B, the density dropped to 1.11×10^9 cm^{-2} with a corresponding Rq value of 0.28 nm. Notably, for sample C, the reduction was even more pronounced with the density dropping to 5.58×10^8 cm^{-2} and an associated Rq value of 0.30 nm. The results suggested that the transition from 3D-to-2D growth mode serves as a driving factor in decreasing surface pit densities. Improved surface morphology aids in mitigating the attenuation of free carrier density at the interface of AlGaN/GaN HEMT due to the scattering effect.

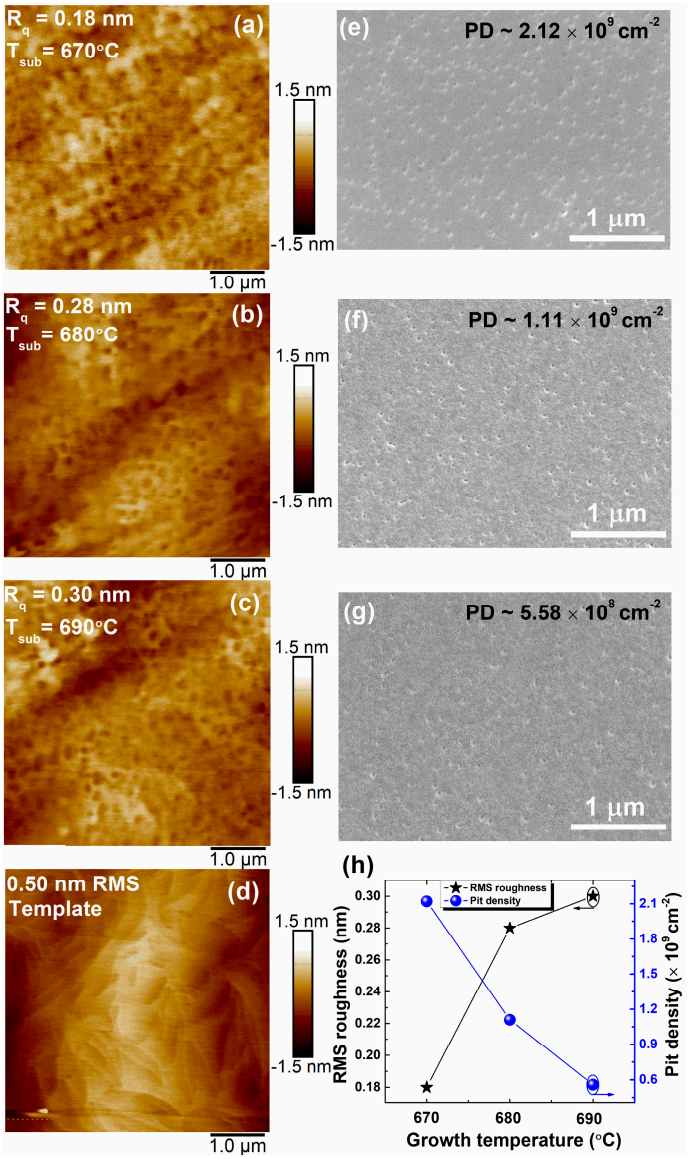

Figure 3. The 5 μm × 5 μm AFM images of the MBE GaN films grown under varied substrate temperatures of (**a**) 670, (**b**) 680, (**c**) 690 °C, and (**d**) MOCVD GaN template. The related SEM images displayed in (**e**–**h**) show the relation between RMS roughness and average surface pit densities plotted against substrate growth temperatures.

3.2. Structural Properties

Figure 4a shows the 2θ XRD patterns of the GaN film grown at 690 °C (sample C). It can be observed that the dominant diffraction peaks corresponding to (100), (002), (102), (003), (103), (004), and (202) planes of the GaN wurtzite structure according to the PDF 01-074-7289 card were detected in all samples (supporting information; see Figure S1). The K_β and K_α Si (111), Si (222), and AlN (002), (004) diffraction peaks arise from the template [32], while the broad and unidentified peak below 20° can be assigned to the X-ray source. The buildup of undesirable impurities in MBE films is anticipated to affect strain generation, leading to modified lattice parameters. Commonly, the relative lattice constants (a and c) were calculated from the peak positions of the common planes (002) and (102) using Bragg's equation [3]:

$$2d_{hkl}\sin\theta_{hkl} = n\lambda \quad (1)$$

$$\frac{1}{d_{hkl}^2} = \frac{4}{3}\left\{\frac{h^2 + hk + k^2}{a^2}\right\} + \frac{l^2}{c^2} \quad (2)$$

where d_{hkl} is the interplanar spacing, which was calculated using Equation (2). The Miller indices (hkl) refer to the respective diffraction planes. θ_{hkl} is the reflection angle. The wavelength λ of the X-ray source is 0.15406 nm. The calculated lattice constants are given in Table 1. These lattice parameters are plotted and compared to those of the fully relaxed GaN values (a_o = 0.3189 nm and c_o = 0.5185 nm) [33], which are illustrated in Figure 4b. It is seen that the computed lattice parameters "a" for all homoepitaxial GaN were found to be slightly greater than the corresponding strain-free GaN value, revealing that GaN films suffered an in-plane tensile strain. This tensile strain typically arises from impurities, defects, and mismatches in the lattice parameters as well as variations in CTE when growing GaN on Si. The results showed that the lattice parameter "a" of the MBE films exhibited a decrease compared to that of the templates, and this reduction became more prominent with increasing Tsub. MOCVD-grown GaN films commonly exhibit a high concentration of free electrons, which is related to the incorporation of undesirable impurities and extended point defects during growth. Such factors probably cause the expansion of the "a" lattice parameter via the size effect [33,34]. Transitioning growth modes are suggested to effectively inhibit the accumulation of undesirable impurities into the growing film, resulting in better MBE GaN crystal quality. Additionally, the presence of Ga droplets has also made it possible to increase thermal expansion coefficients, which could be responsible for expanding the lattice parameter [35]. Indeed, the decrease in lattice parameter "a" in MBE GaN films with rising Tsub demonstrated efficient Ga atom desorption from the surface, which was facilitated by adequate surface desorption energy at a precisely controlled growth temperature. Therefore, the finding indicates that the reduction in lattice parameters can be attributed to either preventing undesirable impurity incorporation and limited extended defects or to the effect of growth temperatures.

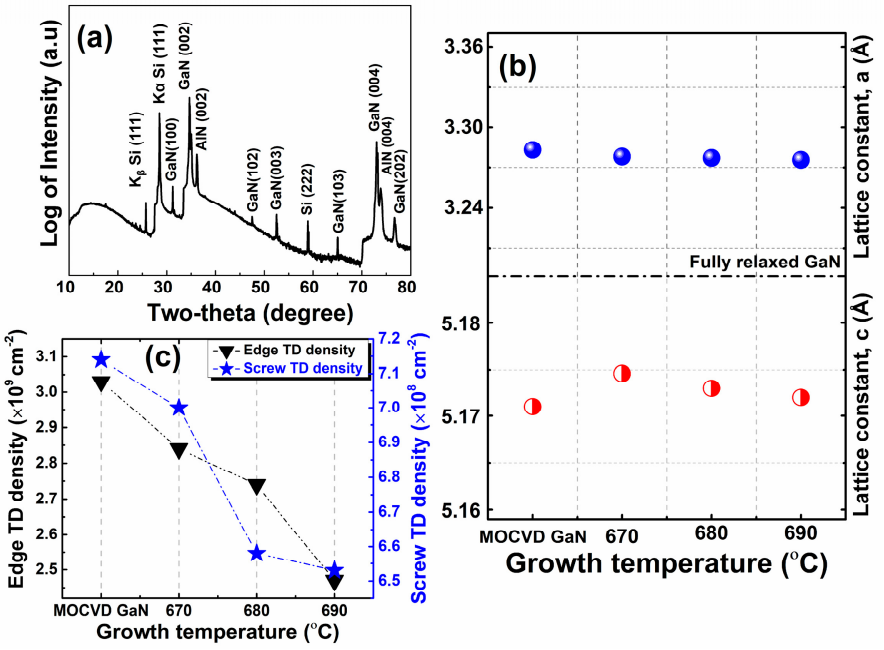

Figure 4. (**a**) The 2θ diffraction peaks of GaN films grown on MOCVD GaN/Si template at 690 °C (sample C), (**b**) variations of "a" (blue balls) and "c" (red balls) lattice parameters, and (**c**) edge (black triangle) and screw (blue star) threading dislocation densities with varied substrate growth temperatures in comparison with MOCVD GaN template.

Table 1. Values of estimated lattice parameters, FWHM extracted from XRD reflections, TDD, PD, RMS, and tensile stress values of MOCVD GaN and MBE GaN films grown at different growth temperatures.

Sample	Growth Temperature (°C)	Lattice Parameters		FWHM (Arcsec)		TDD (cm^{-2})		PD (cm^{-2})	RMS (nm)	Tensile Stress, σ (GPa)
		a (nm)	c (nm)	(002)	(102)	STD	ETD			
X	MOCVD GaN	0.3283	0.5171	596	966	7.14×10^8	3.03×10^9	-	0.51	0.36
A	670	0.3278	0.5174	590	939	7.00×10^8	2.84×10^9	2.12×10^9	0.18	0.31
B	680	0.3277	0.5173	572	889	6.58×10^8	2.74×10^9	1.11×10^9	0.28	0.27
C	690	0.3276	0.5172	570	880	6.53×10^8	2.47×10^9	5.58×10^8	0.30	0.12

The structural quality and reduction in dislocations of GaN films relative to sample X were studied by the X-ray rocking curve near the (002) and (102) reflections. The rocking curves and their broadening for all samples can be found in Figure S2 and Table 1, respectively. The curve broadening is associated with dislocations in the films that can be classified as screw-type dislocation (STD) and edge-type dislocation (ETD). The densities of each type of dislocation were determined through the full-width at half maximum (FWHM) of (002) and (102) reflections from Equations (3) and (4) [10]:

$$D_{screw} = \frac{\beta^2_{(002)}}{4.35 \times b^2_{screw}} \quad (3)$$

$$D_{edge} = \frac{\beta^2_{(102)} - \beta^2_{(002)}}{4.35 \times b^2_{edge}}, \quad (4)$$

where β is the FWHM values recorded for the (002) and (102) reflections. The Burgers vector magnitudes for STD and ETD are identified as b_s = 0.5185 nm and b_e = 0.3189 nm, respectively [36]. The calculated dislocation densities for GaN films are provided in Table 1, and their variation with Tsub is plotted in Figure 4c. The results revealed a considerable reduction in both types of dislocations in MBE GaN when compared to those observed in templates. In addition, with an increasing Tsub, the dislocations decrease further. Specifically, the film grown at 690 °C exhibited the most substantial decrease in dislocation densities compared to other samples. For instance, the estimated TDD of sample C demonstrated a remarkable reduction, lowering by 8.5% for STD and an impressive 18.5% for ETD when compared to the corresponding values in the template. The observed reduction in dislocation densities is basically consistent with the decrease in surface pit densities. The decline in edge dislocations indicates the impact resulting from the growth mode transitioning from 3D to 2D, which was achieved by modulating Tsub. This finding is consistent with our previous research, where the 3D-to-2D growth mode transition was facilitated by employing SiNx interlayers [14]. Threading dislocations were observed to bend at the interface of the growth mode transition with subsequent annihilation occurring during the 2D growth of MBE-grown GaN films. However, as discussed, the use of interlayers introduced potential drawbacks to device performance. Thus, the promoted 3D-to-2D growth mode transition at high growth temperatures via MBE presents a promising approach to minimize further threading dislocations achieved in cases of thin GaN thickness (<6 μm). Furthermore, STD arises from the inclusion of unexpected impurities, which work as a vertical leakage path caused by the charge-trapping phenomenon [9,37]. Meanwhile, ETD works as a Coulomb scattering center, which lessens the carrier mobility and builds up the sheet resistance [8]. Therefore, the significantly decreasing dislocation densities in our work hold promise for meeting the current state-of-the-art power devices for high-efficiency devices [38].

3.3. Optical and Electrical Characteristics

The effectively lowered dislocations are obtained from the initial in-plane stress relaxation, which is further investigated using Raman spectroscopy. Figure 5a illustrates the Raman spectra of GaN films that reveal two identifiable E2(H) and A1(LO) active phonons [10]. The shift in the E2(H) phonon with respect to the stress-free value of 567.5 cm^{-1} (see Figure 5b) is sensitive to the stress existent in GaN films. The E2(H) peak positions of samples X, A, B, and C were 565.92, 566.18, 566.37, and 566.96 cm^{-1}, respectively. The shift in the E2(H) phonon peak to the stress-free direction reflects the relaxation of the endured stress in GaN films, which agrees with the XRD result. The in-plane stress was computed from Equation (5) [10]:

$$\sigma = \frac{\Delta\omega}{4.3}\text{GPa}, \tag{5}$$

where $\Delta\omega$ is the difference between the stress-free peak position and the empirically observed E2(H) positions, and σ is the denotable in-plane stress expressed in GPa. The computed stress values are given in Table 1 and plotted in Figure 5c with the negative sign indicating tensile stress magnitudes. The observed stress relaxation trend (Figure 5c) revealed a gradual alleviation of residual tensile stress in GaN templates as compared to MBE-grown GaN. The effectiveness of stress release significantly improved with higher Tsub. Particularly notable is the substantial residual stress relaxation observed in GaN grown at 690 °C, resulting in a noteworthy reduction to 0.12 GPa. This suggests that the precise control of growth temperatures significantly contributes to stress relaxation during the 2D coalescence of MBE GaN films, consequently leading to decreased dislocation densities. The manifestation of this characteristic was evident in the improved surface morphologies observed through AFM along with low surface pit densities in MBE GaN. The stress relaxation also contributes to minimizing wafer cracking and bowing, especially in large-wafer-size manufacturing, ultimately improving device performance in GaN-based HEMT applications.

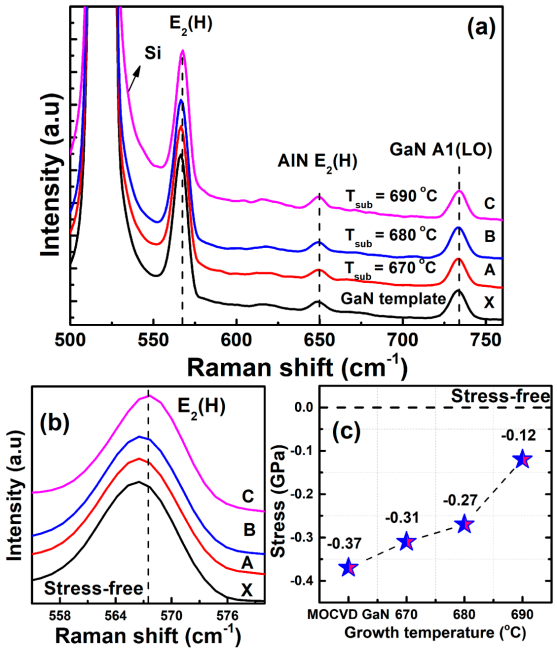

Figure 5. (**a**) Raman spectra of all GaN films; (**b**) Raman spectra in E2(H) regions; (**c**) the stress values (star-dashed line) displayed as a function of substrate growth temperature relative to the MOCVD template.

The influence of Tsub on luminescence properties was investigated through low-temperature photoluminescence spectra performed at 10 K, as shown in Figure 6. A sharp and narrow dominant near band-edge (NBE) emission associated with the exciton-bound neutral donor (D^0X) peak along with their LO-phonon replicas was observed at around 3.45 eV [39]. Samples X, A, B, and C had maximum D^0X peaks of 3.465, 3.466, 3.467, and 3.469 eV and corresponding FWHM values of 13.9, 16.1, 15.7, and 13.5 meV, respectively. The blueshift in D^0X emission peaks was toward the stress-free value of 3.471 eV for relaxed GaN film [39], which confirms the tensile stress relaxation.

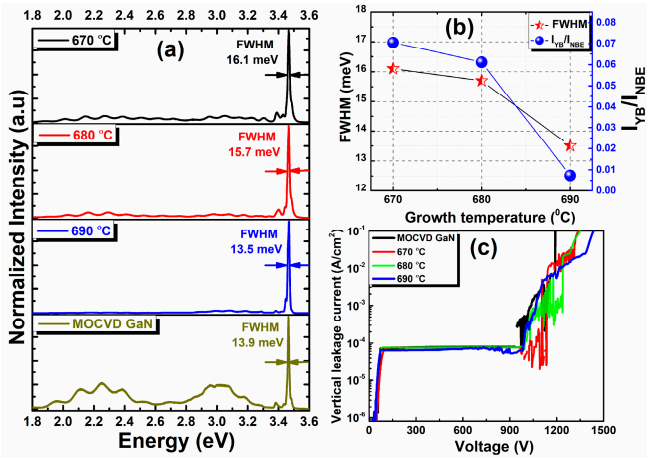

Figure 6. (**a**) The 10K PL spectra for MBE GaN grown at varying substrate temperatures in comparison with MOCVD GaN, (**b**) the full width at half maximum (FWHM) and the PL intensity ratio of I_{YB}/I_{NBE} of MBE GaN plotted as a function of growth temperatures. (**c**) Vertical leakage current versus voltage curves of GaN films.

Figure 6a shows that the MOCVD GaN exhibited the pronounced emissions of defect-related broad yellow luminescence (YL) and blue luminescence (BL) bands that were observed at around 2.2 eV and 2.8–3.0 eV, respectively [40,41]. The origin of YL and BL emissions is widely established as the attributions of edge-type dislocation [42], gallium vacancy (V_{Ga}) [43], and impurity-related complex defects [44]. It is noteworthy that the MBE GaN exhibited a remarkable decrease in both YL and BL emissions. In particular, the film grown at 690 °C completely eliminated the YL intensity and exhibited a sharper NBE emission (see Figure 6b). The findings demonstrated that the 3D to 2D growth mode transition established by modulating Tsub is advantageous in improving both their structure quality and optical properties. These characteristics were further investigated by evaluating the relative intensity ratio of the YL band to NBE emission (I_{YB}/I_{NBE}). Figure 6b plots the FWHM values of NBE emissions and I_{YB}/I_{NBE} as a function of Tsub. The results revealed that the I_{YB}/I_{NBE} ratio went down and NBE emissions became narrower as Tsub increased, affirming an improvement in film quality. Clearly, the XRD results indicated that MBE GaN films have exhibited a notable decrease in both types of dislocations with a more significant drop observed in ETD. However, this study illustrates that GaN films with the best surface morphology do not always result in the best luminescence properties. It proves the importance of controlling the growth temperature even when achieving the best-attained surface smoothness. In particular, the smoothest surface morphology found in GaN film grown at 670 °C, due to the residual Ga atoms, did not demonstrate the promising luminescence properties found in GaN grown at 690 °C. The slight remaining Ga atoms on the surface might potentially be ascribed to the YL emission. Therefore, the reduced YL intensity with the increase in Tsub can be a result of efficiently desorbing the remaining Ga atoms on the film surface by the inherent substrate thermal energy. Previously, Turkulets et al. [45] also identified the contribution of a certain molecule surface to the YL emission. The collective findings suggest that the Tsub of 690 °C can be considered

the optimal growth temperature for high-quality MBE films with anticipated improvements in electrical properties.

It should be mentioned that MOCVD-grown GaN films frequently come with a considerable background of undesirable impurities [7]. The incorporation of impurities into the grown film and their buildup to the 2DEG region were proven to be accountable for the leakage current paths and reduced BV [46]. Hence, the impressively diminished defect-related YL emissions observed in MBE films denote an improvement in electrical properties that was examined using I-V measurement.

Figure 6c illustrates the vertical leakage current against the breakdown voltage curves. It is seen that the I–V characteristics observed in the 0–950 V range are attributed to the responses of C-doped GaN/AlGaN/AlN/Si [47]. Within a low applied voltage range of 0–75 V, the vertical leakage current climbed from 10^{-6} to 10^{-4} A/cm^2. Subsequently, once the applied voltage was raised to ~950 V, the leakage current value remained constant at 10^{-4} A/cm^2. Then, a rise in the vertical leakage current was observed when the applied voltage progressed from ~950 V to the highest BV value. The I–V characteristic in this region predominantly reflects the response of the top UID GaN layers. Hence, we primarily discuss the I–V behaviors in this region to assess the improved electrical properties of MBE-grown GaN layers. The applied voltage at which the vertical leakage current was 0.1 A/cm^2 is referred to as the BV value for all samples. The values of BV were found to be 1180, 1320, 1350, and 1450 V for samples X, A, B, and C, respectively. Clearly, all MBE-grown GaN samples exhibited a significant BV enhancement compared to the template. The greater breakdown voltage in MBE GaN is a result of both increased growth thickness and improved crystal quality [48]. In addition, the distinctly noisy vertical leakage characteristics observed in MBE GaN films grown at 670 °C and 680 °C, as well as in the template, could be attributed to the high densities of dislocations and surface pits [49,50]. Moreover, the origin of the failing electrical properties in samples A and B can be traced to the remaining surface Ga atoms and the nitrogen vacancy that act as interfacial defects and buffer traps. Notably, the noise-free vertical leakage current observed in the GaN grown at 690 °C resulted from a better surface morphology contributed by a tailor growth temperature.

It has been found that MBE-grown GaN films unveil a remarkable improvement in both vertical leakage current and BV compared to our prior study on MOCVD-grown GaN-based HEMTs [19]. The MBE GaN films exhibited excellent electrical properties, illustrating a current leakage of 0.1 A/cm^2 at an impressive BV of 1450 V. It showed a substantial enhancement over the previous MOCVD GaN structure, which exhibited a current leakage of 10 A/cm^2 at a BV of 1000 V. Remarkably, the growth mode transition technique significantly enhances the buffer breakdown voltage in thin MBE GaN (1.9 μm) compared to that of standard-sized GaN HEMT structures (5 μm). For instance, the breakdown voltages reported in different GaN structural designs were approximately 800 V [51], 900 V [52], and 1000 V [53] measured at a current density of 0.1 A/cm^2. The marked improvement is attributed to reduced edge threading dislocations contributed by 3D-to-2D growth mode transition in MBE GaN and a lower incorporation of donor-like impurities into film during coalescence. It not only highlights the advantages of using the MBE approach to perform 3D-to-2D growth mode transition and overcome impurity issues but also establishes it as the superior choice for enhanced electrical performance in GaN-based devices.

4. Conclusions

Our investigation into the MBE-grown UID GaN channel layer on MOCVD GaN templates with precise control over substrate growth temperatures has revealed significant advancements in crystal quality as well as morphological, optical, and electrical properties during the transition from 3D island to 2D growth mode. The optimal film quality was achieved at a growth temperature of 690 °C. The resulting relaxed strained MBE GaN film quality exhibited notably reduced edge dislocations and surface pit densities, measuring as

low as 2.47 × 10^9 cm^{-2} and 5.58 × 10^8 cm^{-2}, respectively. Moreover, the tailored growth temperature conditions delivered an improved surface roughness (Rq = 0.3 nm), indicating an efficient prevention of surface desorption at elevated Tsub. The enhanced crystalline quality resulted in improved luminescence properties characterized by a narrower NBE emission band and a pronounced reduction in trap-related YL emission intensity. Furthermore, the optimized MBE-grown sample exhibited highly attractive electrical properties, featuring noise-free vertical leakage current characteristics under high applied voltage operations (BV~1450 V). The findings emphasize the efficacy of controlling MBE growth temperature to promote growth mode transition for optimizing GaN channel layer properties. It holds immense promise for achieving high efficiency and power for GaN-on-Si transistor applications. Our work collectively contributes to advancing the understanding of growth parameters in pursuing optimal GaN-based HEMT for next-generation semiconductor devices.

Supplementary Materials: The following supporting information can be downloaded at https://www.mdpi.com/article/10.3390/coatings14020191/s1, Figure S1: The 2-theta diffraction patterns of MBE-grown GaN films and the MOCVD GaN/Si template; Figure S2: X-ray rocking curves of all GaN films scanned on (a) (002) and (b) (102) reflections.

Author Contributions: T.T.M. conceived and designed the experiments, performed the epitaxial growth, analyzed the results, and wrote the manuscript. J.-J.D. supported the MOCVD GaN templates and analyzed the results. L.T.H. supported the I–V characterization. H.-C.W. supported the morphology observation. W.-C.C. is the advisor who supervised the experiments and revised the manuscript. H.H.L. discussed the results and revised the manuscript. All authors have analyzed the data, discussed the data, and revised the manuscript. All authors have read and agreed to the published version of the manuscript.

Funding: This research was funded by the National Science and Technology Council, Taiwan, under grant No. NSTC 112-2112-M-A49-399-043 and NSTC 112-2218-E-A49-018.

Institutional Review Board Statement: Not applicable.

Informed Consent Statement: Not applicable.

Data Availability Statement: Data are contained within the article or Supplementary Materials.

Conflicts of Interest: The authors declare no conflicts of interest.

References

1. Kim, J.-G.; Cho, C.; Kim, E.; Hwang, J.S.; Park, K.-H.; Lee, J.-H. High breakdown voltage and low-current dispersion in AlGaN/GaN HEMTs with high-quality AlN buffer layer. *IEEE Trans. Electron Devices* **2021**, *68*, 1513–1517. [CrossRef]
2. Ma, J.; Matioli, E. High-voltage and low-leakage AlGaN/GaN tri-anode Schottky diodes with integrated tri-gate transistors. *IEEE Electron Device Lett.* **2016**, *38*, 83–86. [CrossRef]
3. Romanitan, C.; Mihalache, I.; Tutunaru, O.; Pachiu, C. Effect of the lattice mismatch on threading dislocations in heteroepitaxial GaN layers revealed by X-ray diffraction. *J. Alloys Compd.* **2021**, *858*, 157723. [CrossRef]
4. Buffolo, M.; Caria, A.; Piva, F.; Roccato, N.; Casu, C.; De Santi, C.; Trivellin, N.; Meneghesso, G.; Zanoni, E.; Meneghini, M. Defects and reliability of GaN-based LEDs: Review and perspectives. *Phys. Status Solidi* **2022**, *219*, 2100727. [CrossRef]
5. Chatterjee, A.; Khamari, S.K.; Kumar, R.; Porwal, S.; Bose, A.; Sharma, T. Role of threading dislocations and point defects in the performance of GaN-based metal-semiconductor-metal ultraviolet photodetectors. *Superlattices Microstruct.* **2020**, *148*, 106733. [CrossRef]
6. Joh, J.; Del Alamo, J.A. A current-transient methodology for trap analysis for GaN high electron mobility transistors. *IEEE Trans. Electron. Devices* **2010**, *58*, 132–140. [CrossRef]
7. Reshchikov, M.; Vorobiov, M.; Andrieiev, O.; Ding, K.; Izyumskaya, N.; Avrutin, V.; Usikov, A.; Helava, H.; Makarov, Y. Determination of the concentration of impurities in GaN from photoluminescence and secondary-ion mass spectrometry. *Sci. Rep.* **2020**, *10*, 2223. [CrossRef] [PubMed]
8. Wong, Y.-Y.; Chang, E.Y.; Yang, T.-H.; Chang, J.-R.; Ku, J.-T.; Hudait, M.K.; Chou, W.-C.; Chen, M.; Lin, K.-L. The roles of threading dislocations on electrical properties of AlGaN/GaN heterostructure grown by MBE. *J. Electrochem. Soc.* **2010**, *157*, H746. [CrossRef]
9. Jarndal, A.; Arivazhagan, L.; Nirmal, D. On the performance of GaN-on-silicon, silicon-carbide, and diamond substrates. *Int. J. RF Microw. Comput.-Aided Eng.* **2020**, *30*, e22196. [CrossRef]

10. Lee, H.-P.; Perozek, J.; Rosario, L.; Bayram, C. Investigation of AlGaN/GaN high electron mobility transistor structures on 200-mm silicon (111) substrates employing different buffer layer configurations. *Sci. Rep.* **2016**, *6*, 37588. [CrossRef]
11. Dalapati, P.; Urata, S.; Egawa, T. Investigation of AlGaN/GaN high electron mobility transistors on Silicon (111) substrates employing multi-stacked strained layer superlattice structures. *Superlattices Microstruct.* **2020**, *147*, 106709. [CrossRef]
12. Liu, J.; Huang, Y.; Sun, X.; Zhan, X.; Sun, Q.; Gao, H.; Feng, M.; Zhou, Y.; Ikeda, M.; Yang, H. Wafer-scale crack-free 10 µm-thick GaN with a dislocation density of 5.8×10^7 cm^{-2} grown on Si. *J. Phys. D Appl. Phys.* **2019**, *52*, 425102. [CrossRef]
13. Amano, H.; Iwaya, M.; Kashima, T.; Katsuragawa, M.; Akasaki, I.; Han, J.; Hearne, S.; Floro, J.A.; Chason, E.; Figiel, J. Stress and defect control in GaN using low temperature interlayers. *Jpn. J. Appl. Phys.* **1998**, *37*, L1540. [CrossRef]
14. Dai, J.-J.; Liu, C.-W.; Wu, S.-K.; Huynh, S.-H.; Jiang, J.-G.; Yen, S.-A.; Mai, T.T.; Wen, H.-C.; Chou, W.-C.; Hu, C.-W. Improving Transport Properties of GaN-Based HEMT on Si (111) by Controlling SiH4 Flow Rate of the SiN x Nano-Mask. *Coatings* **2020**, *11*, 16. [CrossRef]
15. Chang, S.; Lung Wei, L.; Tung Luong, T.; Chang, C.; Chang, L. Threading dislocation reduction in three-dimensionally grown GaN islands on Si (111) substrate with AlN/AlGaN buffer layers. *J. Appl. Phys.* **2017**, *122*, 105306. [CrossRef]
16. Tanaka, S.; Honda, Y.; Sawaki, N.; Hibino, M. Structural characterization of GaN laterally overgrown on a (111) Si substrate. *Appl. Phys. Lett.* **2001**, *79*, 955–957. [CrossRef]
17. Strittmatter, A.; Rodt, S.; Reißmann, L.; Bimberg, D.; Schröder, H.; Obermeier, E.; Riemann, T.; Christen, J.; Krost, A. Maskless epitaxial lateral overgrowth of GaN layers on structured Si (111) substrates. *Appl. Phys. Lett.* **2001**, *78*, 727–729. [CrossRef]
18. Zhong, Y.; Zhang, J.; Wu, S.; Jia, L.; Yang, X.; Liu, Y.; Zhang, Y.; Sun, Q. A Review on the GaN-on-Si Power Electronic Devices. *Fundam. Res.* **2021**, *2*, 462–475. [CrossRef]
19. Dai, J.-J.; Mai, T.T.; Nallasani, U.R.; Chang, S.-C.; Hsiao, H.-I.; Wu, S.-K.; Liu, C.-W.; Wen, H.-C.; Chou, W.-C.; Wang, C.-P. The effect of heavy Fe-doping on 3D growth mode and Fe diffusion in GaN for high power HEMT application. *Materials* **2022**, *15*, 2058. [CrossRef] [PubMed]
20. Zhang, H.; Xue, J.; Fu, Y.; Yang, M.; Zhang, Y.; Duan, X.; Qiang, W.; Li, L.; Sun, Z.; Ma, X. Study on the effects of growth rate on GaN films properties grown by plasma-assisted molecular beam epitaxy. *J. Cryst. Growth* **2020**, *535*, 125539. [CrossRef]
21. Wu, Y.-Z.; Liu, B.; Li, Z.-H.; Tao, T.; Xie, Z.-L.; Xiu, X.-Q.; Chen, P.; Chen, D.-J.; Lu, H.; Shi, Y. Homo-epitaxial growth of high crystal quality GaN thin films by plasma assisted–molecular beam epitaxy. *J. Cryst. Growth* **2019**, *506*, 30–35. [CrossRef]
22. Heying, B.; Averbeck, R.; Chen, L.; Haus, E.; Riechert, H.; Speck, J. Control of GaN surface morphologies using plasma-assisted molecular beam epitaxy. *J. Appl. Phys.* **2000**, *88*, 1855–1860. [CrossRef]
23. Liang, K.; Sun, X.; Wu, G.; Zhang, L.; Liu, S.; Gan, Z. The investigation of molecular beam epitaxy growth of GaN by molecular dynamics simulation. *Comput. Mater. Sci.* **2020**, *173*, 109426. [CrossRef]
24. Shrestha, N.M.; Li, Y.; Suemitsu, T.; Samukawa, S. Electrical characteristic of AlGaN/GaN high-electron-mobility transistors with recess gate structure. *IEEE Trans. Electron Devices* **2019**, *66*, 1694–1698. [CrossRef]
25. Cao, Y.; Xing, H.; Jena, D. Polarization-mediated remote surface roughness scattering in ultrathin barrier GaN high-electron mobility transistors. *Appl. Phys. Lett.* **2010**, *97*, 222116. [CrossRef]
26. Kruse, C.; Einfeldt, S.; Böttcher, T.; Hommel, D.; Rudloff, D.; Christen, J. Spatially modified layer properties related to the formation of gallium droplets on GaN (0001) surfaces during plasma-assisted molecular-beam epitaxy. *Appl. Phys. Lett.* **2001**, *78*, 3827–3829. [CrossRef]
27. Sampath, A.; Garrett, G.; Collins, C.; Boyd, P.; Choe, J.; Newman, P.; Shen, H.; Wraback, M.; Molnar, R.; Caissie, J. Effect of Ga-rich growth conditions on the optical properties of GaN films grown by plasma-assisted molecular beam epitaxy. *J. Vac. Sci. Technol. B Microelectron. Nanometer Struct. Process. Meas. Phenom.* **2004**, *22*, 1487–1490. [CrossRef]
28. Krishna, S.; Aggarwal, N.; Mishra, M.; Maurya, K.; Singh, S.; Dilawar, N.; Nagarajan, S.; Gupta, G. Correlation of growth temperature with stress, defect states and electronic structure in an epitaxial GaN film grown on c-sapphire via plasma MBE. *Phys. Chem. Chem. Phys.* **2016**, *18*, 8005–8014. [CrossRef] [PubMed]
29. Adelmann, C.; Brault, J.; Jalabert, D.; Gentile, P.; Mariette, H.; Mula, G.; Daudin, B. Dynamically stable gallium surface coverages during plasma-assisted molecular-beam epitaxy of (0001) GaN. *J. Appl. Phys.* **2002**, *91*, 9638–9645. [CrossRef]
30. Able, A.; Wegscheider, W.; Engl, K.; Zweck, J. Growth of crack-free GaN on Si (1 1 1) with graded AlGaN buffer layers. *J. Cryst. Growth* **2005**, *276*, 415–418. [CrossRef]
31. Smith, A.; Ramachandran, V.; Feenstra, R.; Greve, D.; Ptak, A.; Myers, T.; Sarney, W.; Salamanca-Riba, L.; Shin, M.; Skowronski, M. Surface reconstruction during molecular beam epitaxial growth of GaN (0001). *Mater. Res. Soc. Internet J. Nitride Semicond. Res.* **1998**, *3*, e12. [CrossRef]
32. Krishna, S.; Aggarwal, N.; Gundimeda, A.; Sharma, A.; Husale, S.; Maurya, K.; Gupta, G. Correlation of donor-acceptor pair emission on the performance of GaN-based UV photodetector. *Mater. Sci. Semicond. Process.* **2019**, *98*, 59–64. [CrossRef]
33. Darakchieva, V.; Monemar, B.; Usui, A. On the lattice parameters of GaN. *Appl. Phys. Lett.* **2007**, *91*, 031911. [CrossRef]
34. Van de Walle, C.G. Effects of impurities on the lattice parameters of GaN. *Phys. Rev. B* **2003**, *68*, 165209. [CrossRef]
35. Moram, M.; Vickers, M. X-ray diffraction of III-nitrides. *Rep. Prog. Phys.* **2009**, *72*, 036502. [CrossRef]
36. Weyher, J.v.L.; Lazar, S.; Macht, L.; Liliental-Weber, Z.; Molnar, R.; Müller, S.; Sivel, V.; Nowak, G.; Grzegory, I. Orthodox etching of HVPE-grown GaN. *J. Cryst. Growth* **2007**, *305*, 384–392. [CrossRef]

37. Besendörfer, S.; Meissner, E.; Lesnik, A.; Friedrich, J.; Dadgar, A.; Erlbacher, T. Methodology for the investigation of threading dislocations as a source of vertical leakage in AlGaN/GaN-HEMT heterostructures for power devices. *J. Appl. Phys.* **2019**, *125*, 095704. [CrossRef]
38. Heuken, L.; Kortemeyer, M.; Ottaviani, A.; Schröder, M.; Alomari, M.; Fahle, D.; Marx, M.; Heuken, M.; Kalisch, H.; Vescan, A. Analysis of an AlGaN/AlN super-lattice buffer concept for 650-V low-dispersion and high-reliability GaN HEMTs. *IEEE Trans. Electron Devices* **2020**, *67*, 1113–1119. [CrossRef]
39. Kornitzer, K.; Ebner, T.; Thonke, K.; Sauer, R.; Kirchner, C.; Schwegler, V.; Kamp, M.; Leszczynski, M.; Grzegory, I.; Porowski, S. Photoluminescence and reflectance spectroscopy of excitonic transitions in high-quality homoepitaxial GaN films. *Phys. Rev. B* **1999**, *60*, 1471. [CrossRef]
40. Reshchikov, M.; Vorobiov, M.; Demchenko, D.; Özgür, Ü.; Morkoç, H.; Lesnik, A.; Hoffmann, M.; Hörich, F.; Dadgar, A.; Strittmatter, A. Two charge states of the C N acceptor in GaN: Evidence from photoluminescence. *Phys. Rev. B* **2018**, *98*, 125207. [CrossRef]
41. Calleja, E.; Sánchez, F.; Basak, D.; Sanchez-Garcia, M.; Munoz, E.; Izpura, I.; Calle, F.; Tijero, J.; Sánchez-Rojas, J.; Beaumont, B. Yellow luminescence and related deep states in undoped GaN. *Phys. Rev. B* **1997**, *55*, 4689. [CrossRef]
42. Zhao, D.; Jiang, D.; Yang, H.; Zhu, J.; Liu, Z.; Zhang, S.; Liang, J.; Li, X.; Li, X.; Gong, H. Role of edge dislocations in enhancing the yellow luminescence of n-type GaN. *Appl. Phys. Lett.* **2006**, *88*, 241917. [CrossRef]
43. Xie, Z.; Sui, Y.; Buckeridge, J.; Sokol, A.A.; Keal, T.W.; Walsh, A. Prediction of multiband luminescence due to the gallium vacancy–oxygen defect complex in GaN. *Appl. Phys. Lett.* **2018**, *112*, 262104. [CrossRef]
44. Lyons, J.; Janotti, A.; Van de Walle, C. Carbon impurities and the yellow luminescence in GaN. *Appl. Phys. Lett.* **2010**, *97*, 152108. [CrossRef]
45. Turkulets, Y.; Shauloff, N.; Chaulker, O.H.; Shapira, Y.; Jelinek, R.; Shalish, I. The GaN (0001) yellow-luminescence-related surface state and its interaction with air. *Surf. Interfaces* **2023**, *38*, 102834. [CrossRef]
46. Borga, M.; Meneghini, M.; Stoffels, S.; Li, X.; Posthuma, N.; Van Hove, M.; Decoutere, S.; Meneghesso, G.; Zanoni, E. Impact of substrate resistivity on the vertical leakage, breakdown, and trapping in GaN-on-Si E-mode HEMTs. *IEEE Trans. Electron. Devices* **2018**, *65*, 2765–2770. [CrossRef]
47. Song, C.; Yang, X.; Ji, P.; Tang, J.; Wu, S.; Xu, Y.; Imran, A.; Wang, M.; Yang, Z.; Xu, F. Impact of Silicon Substrate with Low Resistivity on Vertical Leakage Current in AlGaN/GaN HEMTs. *Appl. Sci.* **2019**, *9*, 2373. [CrossRef]
48. Rowena, I.B.; Selvaraj, S.L.; Egawa, T. Buffer thickness contribution to suppress vertical leakage current with high breakdown field (2.3 MV/cm) for GaN on Si. *IEEE Electron. Device Lett.* **2011**, *32*, 1534–1536. [CrossRef]
49. Tajalli, A.; Borga, M.; Meneghini, M.; De Santi, C.; Benazzi, D.; Besendörfer, S.; Püsche, R.; Derluyn, J.; Degroote, S.; Germain, M. Vertical leakage in GaN-on-Si stacks investigated by a buffer decomposition experiment. *Micromachines* **2020**, *11*, 101. [CrossRef]
50. Choi, F.; Griffiths, J.; Ren, C.; Lee, K.; Zaidi, Z.; Houston, P.; Guiney, I.; Humphreys, C.; Oliver, R.; Wallis, D. Vertical leakage mechanism in GaN on Si high electron mobility transistor buffer layers. *J. Appl. Phys.* **2018**, *124*, 055702. [CrossRef]
51. Borga, M.; Meneghini, M.; Benazzi, D.; Canato, E.; Püsche, R.; Derluyn, J.; Abid, I.; Medjdoub, F.; Meneghesso, G.; Zanoni, E. Buffer breakdown in GaN-on-Si HEMTs: A comprehensive study based on a sequential growth experiment. *Microelectron. Reliab.* **2019**, *100*, 113461. [CrossRef]
52. Chen, X.; Zhong, Y.; Yan, S.; Guo, X.; Gao, H.; Sun, X.; Wang, H.; Li, F.; Zhou, Y.; Feng, M. Enhanced breakdown voltage and dynamic performance of GaN HEMTs with AlN/GaN superlattice buffer. *J. Phys. D Appl. Phys.* **2023**, *56*, 355101. [CrossRef]
53. Tajalli, A.; Meneghini, M.; Besendörfer, S.; Kabouche, R.; Abid, I.; Püsche, R.; Derluyn, J.; Degroote, S.; Germain, M.; Meissner, E. High breakdown voltage and low buffer trapping in superlattice gan-on-silicon heterostructures for high voltage applications. *Materials* **2020**, *13*, 4271. [CrossRef]

Disclaimer/Publisher's Note: The statements, opinions and data contained in all publications are solely those of the individual author(s) and contributor(s) and not of MDPI and/or the editor(s). MDPI and/or the editor(s) disclaim responsibility for any injury to people or property resulting from any ideas, methods, instructions or products referred to in the content.